PREDICTING THE TIME EVOLUTION OF SPACE DEBRIS SPIN PERIOD FOR ACTIVE DEBRIS REMOVAL MISSIONS

Nicola Cimmino[(1)], Alessandro Vananti[(1)], Thomas Schildknecht[(1)]

[(1)] Astronomical Institute, University of Bern, CH-3012 Bern, Switzerland, Email: nicola.cimmino@unibe.ch, alessandro.vananti@unibe.ch, thomas.schildknecht@unibe.ch

ABSTRACT

Predicting the long-term evolution of the spin period of space debris is fundamental to support Active Debris Removal missions. The Astronomical Institute of the University of Bern has conducted optical observations campaigns targeting inactive GLONASS satellites for more than eight years. The observed spin periods, which can be determined from light curves analysis, have revealed various long-term patterns, motivating investigations into the specific initial conditions and physical characteristics of a space object that trigger such behaviours. In this context, this paper presents an extensive sensitivity analysis of the long-term spin period evolution of uncontrolled objects in Medium Earth Orbit against different parameters such as geometry, surface properties, and initial attitude states. The findings from this analysis are then applied to constrain the initial conditions space of a simplified GLONASS model to enable the reproduction of the observed trends with simulations.

1 INTRODUCTION

The increasing population of Resident Space Objects (RSOs) in Earth's orbit, particularly defunct satellites and fragments from breakup events, has intensified the need for Active Debris Removal (ADR) initiatives to ensure the sustainability of space operations [1]. Among the various ADR technologies under consideration, methods necessitating close-proximity interactions with target debris, such as robotic arms [2], harpoons [3], and nets [4] are of particular interest. A key design parameter of these missions is the spin period of the debris, as it directly influences both the approach strategy and the capture mechanism. Underestimating the spin period can increase the collision risk or the structural stress on the ADR mechanism; overestimating it can instead lead to additional fuel and time expense, increasing mission costs. Given that ADR missions typically require a development timeline of 5 to 10 years from early phase to launch [5], it is crucial to anticipate potential changes in the spin characteristics of target debris over this period. The evolution of an object's spin period is influenced by several factors, including its geometric configuration, surface properties, mass distribution, and the specific orbital environment it occupies [6].

Light curves, representing the temporal variations in an object's brightness as observed by optical sensors, are extensively used to determine the spin periods of space objects [7]. Various methodologies have been developed to extract angular velocity or spin period information from light curves, each tailored to specific data characteristics such as observation duration, sampling frequency, data gaps, and uneven time intervals. Spectral analysis techniques [8], including the Fast Fourier Transform, periodogram analysis, and Welch's method, are commonly employed to estimate the power spectral density of a signal, thereby identifying dominant frequency components. A significant limitation of these techniques is their assumption of evenly spaced data points. To address unevenly spaced observations, alternative approaches have been developed such as epoch folding [9], the Lomb-Scargle periodogram [10, 11] and phase reconstruction methods [8]. Lately, machine learning techniques have been increasingly applied to estimate spin periods and characteristics of space objects from light curve data, offering advantages in handling large datasets and complex patterns that traditional methods may struggle with [12].

The Astronomical Institute of the University of Bern (AIUB) has extensive experience in acquiring and processing light curves to estimate the spin periods of RSOs. AIUB operates its observation facility at the Zimmerwald Observatory, located 10 kilometres south of Bern, Switzerland. This facility is equipped with multiple instruments to enable measurements to RSOs, in particular the 1-meter Zimmerwald Laser and Astrometry Telescope (ZIMLAT) and the 0.2-meter Zimmerwald Small Aperture Robotic Telescope (ZimSMART) [13]. Apparent rotational periods and their evolutions have been estimated for various types of RSOs, including box-wing spacecraft, upper stages, and fragmentation debris across different orbital regimes. From 2015 to 2023, AIUB was in particular observing the Russian Global Navigation Satellite System (GLONASS), since the Center for Orbit Determination in Europe (CODE) identified over 70 decommissioned GLONASS satellites. These long-term observations have revealed diverse patterns in the spin period evolution: some satellites exhibit clear annual periodicities, and/or secular trends of the spin period, some feature abrupt changes in the rotational speed, while others show no

Proc. 9th European Conference on Space Debris, Bonn, Germany, 1–4 April 2025, published by the ESA Space Debris Office
Editors: S. Lemmens, T. Flohrer & F. Schmitz, (http://conference.sdo.esoc.esa.int, April 2025)

discernible patterns. Understanding the factors influencing these patterns is crucial for predicting the rotational behaviour of the space debris, which in turn supports the early design phase of ADR missions. Preliminary analyses at AIUB have contributed to this understanding. Notably, reference [14–16] conducted statistical studies on the GLONASS satellite population, deriving metrics such as average spin periods, cycle periods, and rates of secular trends. They also developed empirical models to fit observed data, allowing for the prediction of future spin periods for very specific cases.

In this context, this paper aims to investigate the factors influencing the long-term evolution of spin periods in space debris in Medium Earth Orbit (MEO). An extensive sensitivity analysis is carried out, examining how different geometries, initial attitude states, angular velocities, surface properties, and satellite configurations impact the spin behaviour. For this purpose, a simulation environment has been set up, that includes a meshed model generator of the target debris and an open-source, high-fidelity numerical propagator capable of integrating coupled orbital and attitude dynamics equations, namely Debris Spin/Orbit Simulation Environment (D-SPOSE) [17, 18]. Furthermore, the findings from this analysis are then applied to constrain the initial conditions space of a simplified GLONASS model to enable the reproduction of the observed trends with simulations.

The remainder of this paper is structured as follows. Section 2 provides an overview of the simulation environment, and the force models utilized in our analyses. Section 3 presents the results of the sensitivity analysis conducted across various parameters. Section 4 describes case studies based on GLONASS satellite observations. Finally, Section 5 offers conclusions and discusses potential directions for future research.

2 SIMULATION ENVIRONMENT

To model the long-term pattern of the spin period, an opensource software (i.e., D-SPOSE) has been adopted, which integrates three coupled differential equations. First, the dynamics equation for orbital motion in Earth-Centred Inertial frame [19]:

$$\ddot{\boldsymbol{r}}(t) = -\frac{\mu}{r(t)^3}\boldsymbol{r}(t) + \sum_j \boldsymbol{a}_j(t, \boldsymbol{r}(t), \boldsymbol{v}(t), \boldsymbol{q}(t), \boldsymbol{\omega}(t)) \quad (1)$$

where $\boldsymbol{r}$ is the position as a function of time t, $r = |\boldsymbol{r}|$, $\boldsymbol{v}$ is the velocity, $\boldsymbol{q}$ is the attitude parametrization, chosen here to be a quaternion, $\boldsymbol{q} = [q_0\ \boldsymbol{q}_v^T]^T$, $\boldsymbol{\omega}$ is the angular velocity of the body with respect to the inertial frame, μ is the Earth's gravitational parameter, and $\boldsymbol{a}_j$ represents the additional considered accelerations due to orbital perturbations, which are a function of the rigid body's position, velocity, and attitude state.

Second, the attitude dynamics equation:

$$\boldsymbol{I}\dot{\boldsymbol{\omega}}(t) + \boldsymbol{\omega}(t)^{\times}\boldsymbol{I}\boldsymbol{\omega}(t) = \sum_j \boldsymbol{\tau}_j(t, \boldsymbol{r}(t), \boldsymbol{v}(t), \boldsymbol{q}(t), \boldsymbol{\omega}(t)) \quad (2)$$

where $\boldsymbol{\tau}_j$ represents the external torques, $\boldsymbol{I}$ is the inertia tensor of the rigid body in the centroidal body-fixed frame. The superscript × denotes the skew-symmetric matrix representation of the cross-product.

Finally, the kinematic equation for the absolute orientation of the spacecraft:

$$\dot{\boldsymbol{q}}(t) = \frac{1}{2}\boldsymbol{\Omega}(\boldsymbol{\omega})\boldsymbol{q}(t) \quad (3)$$

where, being ω_x, ω_y and ω_z the angular velocity components in the Body Reference Frame (BRF) [20]:

$$\boldsymbol{\Omega} = \begin{bmatrix} 0 & -\omega_x & -\omega_y & -\omega_z \\ \omega_x & 0 & \omega_z & -\omega_y \\ \omega_y & -\omega_z & 0 & \omega_x \\ \omega_z & \omega_y & -\omega_x & 0 \end{bmatrix} \quad (4)$$

Eqs. 1-3 are numerically propagated at a fixed integration time step using the Runge-Kutta Dormand-Prince numerical integration method [21]. The same time step is used for propagating both the orbital and attitude equations as both are coupled.

The spin period (T) is then computed using the following equation.

$$T(t) = \frac{2\pi}{|\boldsymbol{\omega}(t)|} \quad (5)$$

Four input files are required to run the simulator:

- a Two-Line Elements (TLE) file corresponding to the initial epoch to extract the initial orbital elements (OEl_0).
- a file containing the propagation parameters, among which the propagation time step, the propagation time, and the sampling frequency of the output.
- a file containing the model parameters (i.e., external perturbations). For the MEO regime, the following orbital and attitude perturbations have been considered: asymmetry of the gravitational field (only J2), third body (Sun and Moon), Solar Radiation Pressure (SRP), gravity gradient torque, and SRP torque. Moreover, the initial attitude of the RSO is described as a rotation of the BRF with respect to the Orbital Reference Frame (ORF) [19] with a classical (3-2-1)-sequence of Euler angles: yaw (ψ), pitch (θ) and roll (ϕ). Similarly, the initial angular velocity is expressed in terms of components of $\boldsymbol{\omega}$ in the BRF.
- a file containing information on the RSO geometry. Any RSO shape can be easily considered, as the input consists of a list of

triangular surfaces, each defined by the positions of its three vertices in the BRF, the direction of its inward surface normal, and the optical coefficients in the visible spectrum. In particular, the surface properties are described by the coefficient of specular reflection (ρ), diffusive reflection (δ) and absorption (α). The three coefficients must satisfy the following constraint.

$$\rho + \delta + \alpha = 1 \tag{6}$$

3 SENSITIVITY ANALYSIS

The sensitivity analysis described in this section aims to analyse the dependence of the spin period on several object's properties and initial conditions. The initial orbital state is assumed to be fixed. In particular, the initial orbital elements, namely, semimajor axis (a), eccentricity (e), inclination (i), right ascension of the ascending node (Ω), argument of perigee (ω) and true anomaly (ν), are extracted from the TLE [22] of COSMOS 2140 (NORAD ID: 21217) at epoch 3rd January 2015, 00:52:13 UTC (see Tab. 1). The propagation time is 1825 days, the integration step is 1 s, and the sampling frequency of the output is 1 state/12 h. Three geometries are considered: a panel, a parallelepiped and a box-wing configuration. The panel is modelled as a plane of size 1.0 × 0.8 m along the y (Y_{BRF}) and z (Z_{BRF}) axes of the BRF, meshed with 4 surfaces (Fig. 1a). The mass is 8 kg and the inertia matrix is:

$$\boldsymbol{I} = \begin{bmatrix} 1.09 & 0 & 0 \\ 0 & 0.43 & 0 \\ 0 & 0 & 0.67 \end{bmatrix} kg\ m^2 \tag{7}$$

The parallelepiped has size 3.0 × 1.0 × 0.8 m along the x (X_{BRF}), Y_{BRF} and Z_{BRF} axes of the BRF, meshed with 12 surfaces (Fig. 1b). The mass is 300 kg and the inertia matrix is:

$$\boldsymbol{I} = \begin{bmatrix} 41.0 & 0 & 0 \\ 0 & 241.0 & 0 \\ 0 & 0 & 250.0 \end{bmatrix} kg\ m^2 \tag{8}$$

The box-wing geometry features a central box of size 3.0 × 1.0 × 0.8 m along X_{BRF}, Y_{BRF} and Z_{BRF}, and two panels of size 3.0 × 1.2 m along Y_{BRF} and Z_{BRF} (Fig. 1c), meshed with 20 surfaces. The central box has a mass of 300 kg; each panel has a mass of 21.6 kg. The inertia matrix is:

$$\boldsymbol{I} = \begin{bmatrix} 146.2 & 0 & 0 \\ 0 & 243.6 & 0 \\ 0 & 0 & 352.6 \end{bmatrix} kg\ m^2 \tag{9}$$

The solar panels can have a canting angle with respect to the central box, expressed as a rotation of amplitude β about Y_{BRF}. In Fig. 1c β is 0 °.

For all the geometries, the BRF-axes coincide with the central axes of inertia of the RSO. Moreover, the BRF is initially aligned as follows: X_{BRF} is along the x axis of the ORF, Y_{BRF} is along the $-y$ axis of the ORF, Z_{BRF} is along the $-z$ axis of the ORF.

For each geometry, the following settings have been explored (see Tab. 2):

- 4 initial attitudes: one assumes that there is no rotation of the BRF with respect to the ORF, and three assume a 90 ° rotation of yaw, pitch and roll respectively.
- 5 initial angular velocities: one assumes that the initial angular velocity is zero. This is representative of a very low speed case. Then, three assume an angular velocity of 5 °/s along each axis of inertia respectively. Finally, it is assumed an angular velocity component of 3.0 °/s along all the three axes of inertia, resulting in $|\boldsymbol{\omega}(t)|$ equal to 5.2 °/s.
- 3 surface properties distributions, namely, all surfaces have either specular reflection (AS), diffusive reflection (AD) or absorption (AA) properties. Additional asymmetric distributions have been considered for the different geometries as will be detailed later in this section.

For the box-wing geometry, the variation of the canting angle has also been explored. Two configurations are considered: a symmetric one in which both panels are rotated of the same angle β, and an asymmetric case in which the left and right solar panels are rotated of β and $-\beta$ respectively.

For each simulated scenario, the mean (μ), median (m) and standard deviation (σ) of the spin period over the whole propagation time (i.e., 1825 days) has been computed.

Table 1. OEl_0 for the sensitivity analysis.

a [km]	e [-]	i [°]	Ω [°]	ω [°]	ν [°]
25505.7	0.002	64.3	89.4	216.6	58.9

Table 2. Model parameters for the sensitivity analysis.

Parameters	Values
$[\psi\ \theta\ \phi]$ °	[0 0 0], [90 0 0], [0 90 0], [0 0 90]
$[\omega_x\ \omega_y\ \omega_z]$ °/s	[0 0 0], [5 0 0], [0 5 0], [0 0 5], [3 3 3]
$[\rho\ \delta\ \alpha]$	[1 0 0], [0 1 0], [0 0 1]
β °	symmetric: $\{0, 45, 90, 135\}$ asymmetric: $\{5, 10, 15\}$

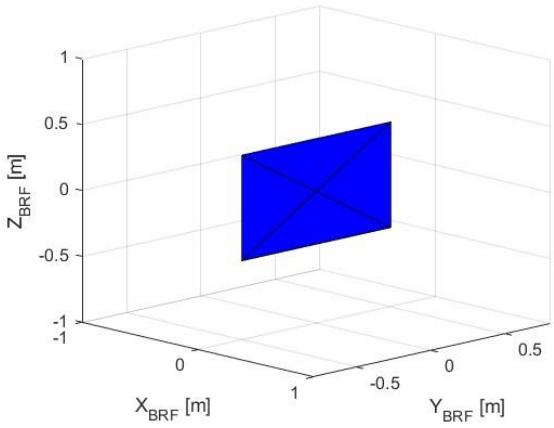

(a)

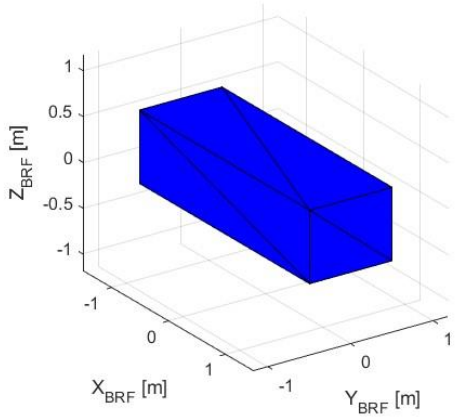

(b)

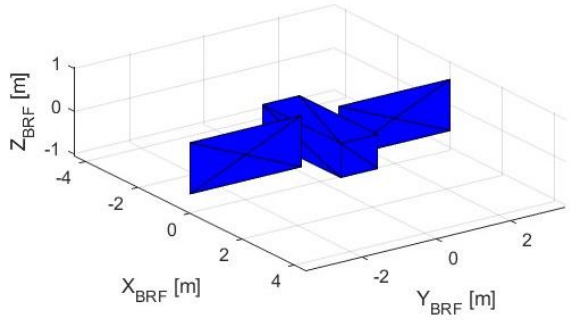

(c)

Figure 1. Meshed model of the panel (a), the parallelepiped (b) and the box-wing geometry (c).

First, results for symmetric geometries and surface properties are presented. Fig. 2 shows the median of the spin period, for the three geometries, assuming $[\rho\ \delta\ \alpha] = [0\ 1\ 0]$ (i.e., AD case), $[\omega_x\ \omega_y\ \omega_z] = [0\ 0\ 0]\ °/s$ (i.e., low-speed case, LoS), and for all the initial attitude states, i.e., $[\psi\ \theta\ \phi]$ equal to $[0\ 0\ 0]$ ° (Zero Attitude, ZA), $[90\ 0\ 0]$ ° (Y_{90}), $[0\ 90\ 0]$ ° (P_{90}), and $[0\ 0\ 90]$ ° (R_{90}). For the box-wing geometry it is reported the configuration for $\beta = 0$ °. Similar results are obtained for the AS and AA cases. Moreover, for the box-wing geometry, similar results are obtained for β equal to 45 °, 90 ° and 135 °. It can be noted that the spin period has a median value bounded between 6 h and 9 h. No significant differences, in terms of values, are observed between the three geometries. It is important to highlight that, regardless of the geometry, the minimum period (i.e., maximum angular speed) is exhibited when the minimum axis of inertia is normal to the orbital plane and the maximum axis of inertia is along the radial direction (z-axis of the ORF). The maximum period (i.e., minimum angular speed) is exhibited when the minimum axis of inertia is along the radial direction (z-axis of the ORF) and the maximum axis of inertia is aligned with the along-track direction.

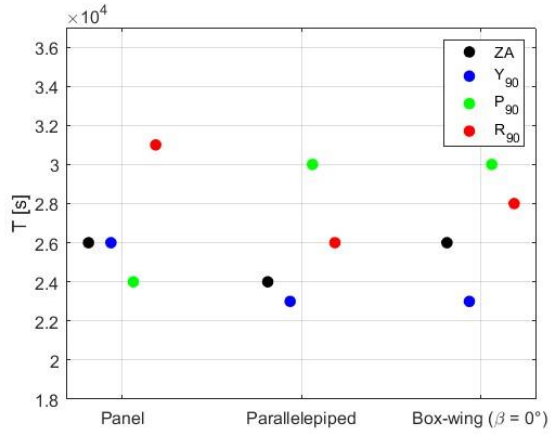

Figure 2. Median of the spin period for the low-speed case, for all the initial attitudes and geometries.

Fig. 3 shows the error bars (i.e., $\mu \pm \sigma$) of the spin period, for the three geometries, assuming $[\rho\ \delta\ \alpha] = [0\ 1\ 0]$ (i.e., AD case). The initial angular velocity has a non-zero component along the maximum axis of inertia (diamond markers) (MaIS) and along the medium axis of inertia (dot markers) (MeIS). The former corresponds to $[\omega_x\ \omega_y\ \omega_z] = [5\ 0\ 0]\ °/s$ for the panel and $[\omega_x\ \omega_y\ \omega_z] = [0\ 0\ 5]\ °/s$ for the parallelepiped and the box-wing geometries. The latter corresponds to $[\omega_x\ \omega_y\ \omega_z] = [0\ 0\ 5]\ °/s$ for the panel and $[\omega_x\ \omega_y\ \omega_z] = [0\ 5\ 0]\ °/s$ for the other two geometries. All the initial attitude states are reported. Regarding the surface properties, similar results are obtained for the AS and AA cases. Regarding the box-wing geometry, similar results are obtained for the other values of β. Moreover, similar considerations to the MaIS case can be made for the case in which the initial angular velocity has a non-zero component along the minimum axis of inertia

(MiIS); similar considerations to the MeIS case can be made for the case in which the initial angular velocity has a non-zero component along all the axes (AllS). It can be noted that for MaIS (and hence for MiIS) the spin period keeps a constant value equal to the initial one for the whole propagation time ($\sigma \sim 10^{-5}$). This is due to the symmetry of the model in terms of geometry, mass distribution and surface properties. For MeIS (and hence for AllS), the spin period has a σ which is smaller than 3% of the mean value. Therefore, also for a non-zero initial angular velocity, the period remains bounded within a narrow interval.

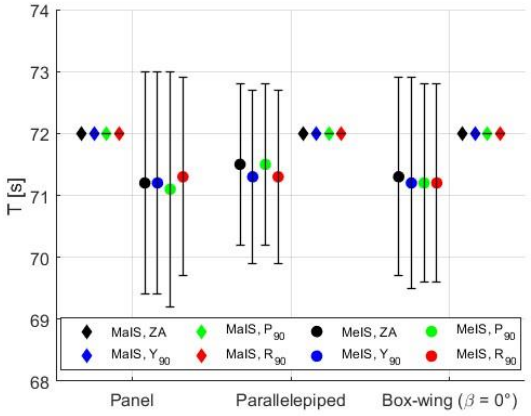

Figure 3. Error bars of the spin period for initial angular velocity along the maximum axis of inertia (MaIS) and the medium axis of inertia (MeIS).

In the next analysis asymmetries in the surface properties of the three geometries are introduced. For the panel, it is assumed that the frontal surface (+X) is AA and the rear surface (-X) is AD. For the parallelepiped it is assumed that the +X surface is AS and all the remaining surfaces are AD. For the box-wing geometry it is assumed that the central box is AD; the solar panels have +X surfaces with AA properties and -X surfaces with AD properties. For all the geometries, there is a significant variation of the spin period in the LoS case. Fig. 4 shows the median values of T for the box-wing geometry with initial P_{90} attitude for symmetric (dots) and asymmetric (diamond) surface properties. This is the case which exhibits the largest variation, with a drop of almost 50% of T. For the remaining initial angular speed cases (i.e., MiIS, MeIS, MaIS, AllS), no significant variation of T is exhibited.

3.1 Asymmetric canting angle

In [14], a feature which has been preliminarily investigated, for a box-wing configuration, is the asymmetry of the canting angle, i.e., the left and right solar panels are canted with a β and $-\beta$ angle respectively. This feature has been further explored in this paper. In particular, β has been set equal to $5\,°, 10\,°$ and $15\,°$. Fig. 5 shows the logarithm base 10 of the median values of T for all the initial attitude states, assuming an AS case and β equal to 5 °. In can be noted that for LoS there is a large reduction of the spin period, and for MeIS and AllS a small reduction of T. On the contrary, for MiIS and MaIS a large increase of T is exhibited. It is important to highlight that, even when the median value of T does not change significantly (as for the MeIS and AllS cases), the pattern of the angular velocity is quite different to the corresponding symmetric case. In fact, in this latter case, the total angular speed is rather constant for the whole observation time, as it can be inferred from the σ values in Fig. 3. When the canting angle of the two panels is asymmetric, a very different pattern is exhibited. Fig. 6 shows the angular velocity components and magnitude of the total angular speed for the AS, P_{90}, MeIS case. An important feature can be observed, i.e., a yearly periodicity, which can be attributed to the apparent motion of the Sun. Moreover, it can be noted a continuous exchange of the angular velocity from the ω_x to the ω_z component.

Introducing an asymmetry in the surface properties as described before leads to a (further) reduction of the spin period for all the cases (see Fig. 7). In fact, such an asymmetry, together with an asymmetric canting angle, induces a secular trend of the angular speed and, hence, of the spin period. Fig. 8 shows the angular speed components and magnitude of the total angular speed for P_{90}, MeIS and asymmetric surface properties. In this case, there is a secular trend of the angular speed and a certain yearly periodicity can be still observed. Moreover, there is a continuous increase of the ω_x component whereas the ω_y and ω_z components vary around a mean zero value.

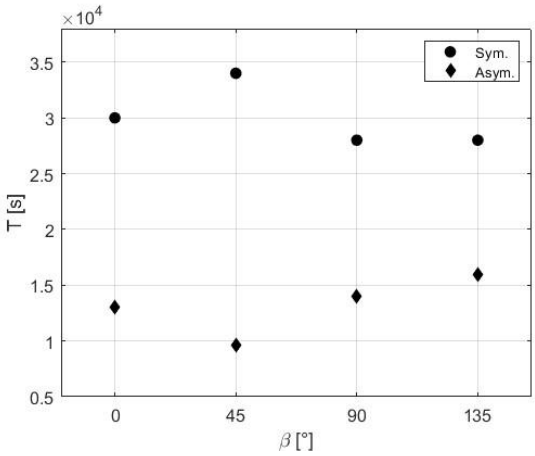

Figure 4. Symmetric β - Median values of the spin period for the box-wing geometry with initial P_{90} attitude, for symmetric (dots) and asymmetric (diamond) surface properties.

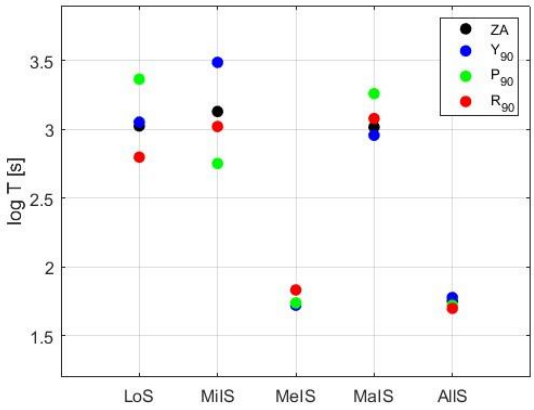

Figure 5. Asymmetric β - Logarithm base 10 of the median values of the spin periods for all the initial attitude states, all-specular (AS) case and β = 5 °.

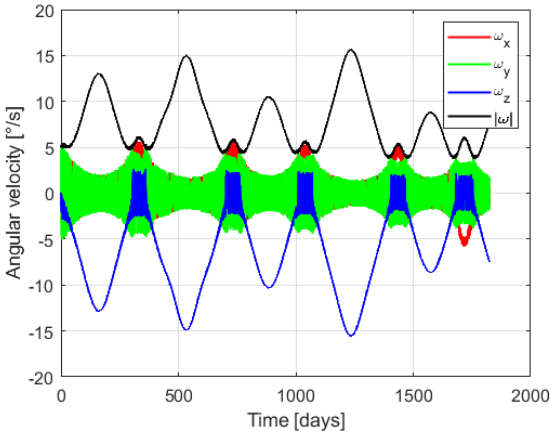

Figure 6. Asymmetric β - Angular velocity for the all-specular (AS) case, a pitch rotation of 90 ° (P_{90}) and initial speed along the medium axis of inertia (MeIS).

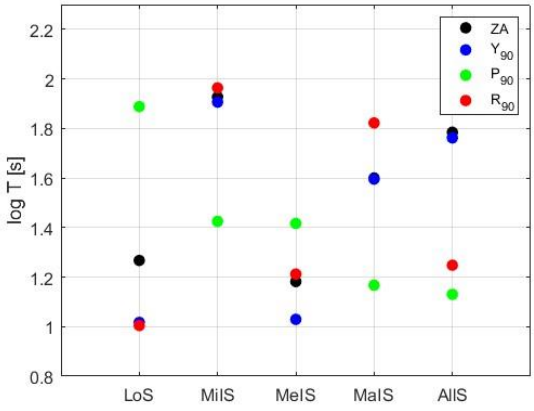

Figure 7. Asymmetric β - Logarithm base 10 of the median values of the spin periods for all the initial attitude states, asym. surface properties and β = 5 °.

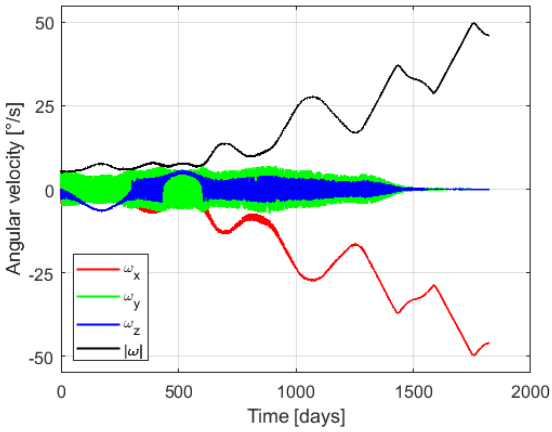

Figure 8. Asymmetric β - Angular velocity for asym. surface properties, a pitch rotation of 90 ° (P_{90}) and initial speed along the medium axis of inertia (MeIS).

Finally, when increasing the canting angle to 10 ° and 15 ° the same considerations apply and the spin period further increases/decreases for most of the cases. This can be observed in Fig. 9 in which it is compared the median values of T, expressed in logarithm base 10, for β equals to 5 ° (dots) and 10 ° (diamonds).

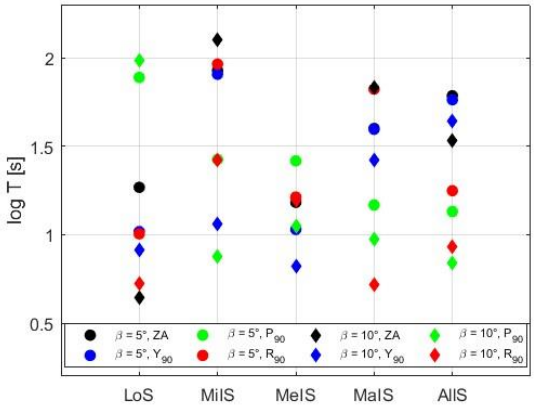

Figure 9. Asymmetric β - Logarithm base 10 of the median values of the spin periods for all the initial attitude states, all-specular surface properties, and β = 5 ° (dots) and 10 ° (diamonds).

4 ANALYSIS OF THE SPIN PERIOD OF INACTIVE GLONASS SATELLITES

A specific observation target at Zimmerwald has been a set of GLONASS satellites [23, 24] which, during the operational life, maintain their orientation using a yaw-steering attitude control mode [25]. The AIUB database contains over 1,800 light curves representing 70 GLONASS satellites. Analysis of these light curves indicates that approximately 83% exhibit patterns where

rotation apparent periods (P_a) can be determined relatively easily [14, 15]. Four different patterns of P_a can be identified: I) monotonic decreasing trend (Fig. 10a), II) oscillating pattern with no secular trend (Fig. 11a), III) oscillating pattern with increasing/decreasing secular trend (Fig. 12a), IV) no pattern. Moreover, in some cases, an abrupt variation of P_a can be observed, featuring a *triangular* shape, as in Fig. 11a and Fig. 12a. To model the first three patterns, i.e., I), II) and III), within the simulation environment, a simplified meshed model of a GLONASS I satellite has been generated [26]. The spacecraft has been modelled as a box-wing satellite with the following characteristics: a central box of size 4.0 × 2.0 × 2.0 m and two solar panels of size 0.0 × 3.5 × 4.0 m. The solar panels have an initial β equal to 0 ° with respect to the central box. The total mass of the satellite is 1400 kg [26] and the inertia matrix is:

$$\boldsymbol{I} = \begin{bmatrix} 1709.5 & 0 & 0 \\ 0 & 2305.3 & 0 \\ 0 & 0 & 2915.2 \end{bmatrix} kg\, m^2 \qquad (10)$$

The initial orbital parameters are extracted from the TLE of COSMOS 2109 (NORAD ID: 21006) at epoch 29th June 2015, 16:29:34 UTC (see Tab. 3) [22].

Table 3. OEl_0 of COSMOS 2109 (NORAD ID: 21006).

a [km]	e [-]	i [°]	Ω [°]	ω [°]	ν [°]
25509.4	0.0082	64.1	208.8	186.2	339.0

Considering the results of the sensitivity analysis, a necessary condition for all the three patterns is to introduce an asymmetry in the geometry. Therefore, an asymmetric canting angle of 5 ° has been set. Modelling parameters for the three patterns are reported in Tab. 4. In particular, for the first case it is necessary to introduce an asymmetry in the surface properties, whose optical values have been tuned, and to have an initial yaw rotation of 90 °. Fig. 10b shows the time evolution of T for the simulated case. In the second test case, as no secular trend is observed, it is assumed that all the surfaces have absorption properties (AA); in fact, only in this case, the triangular feature is exhibited in the simulated period. Fig. 11b shows the time evolution of T for the simulated case. In the last case, surface properties are set as in case I), as a secular trend is observed again. Nevertheless, a combination of the oscillating pattern and the secular trend is observed for a different initial attitude, i.e., a rotation of 90 ° around the roll axis. Fig. 12b shows the time evolution of T for the simulated case.

For all the cases, the main features of the patterns have been captured by the simulation results, namely monotonic decreasing pattern for I), periodic oscillating pattern and triangular shape for II), and periodic pattern with secular trend for III). Nevertheless, a few differences can be noticed when comparing observed and simulated data. This includes the amplitude of the oscillations and the slope of the secular trend. Such discrepancies can be attributable to the initial set of the modelling parameters as well as to mismatches in the geometric and mass distribution properties of the modelled spacecraft.

Table 4. Modelling parameters for GLONASS satellites analysis.

	$[\rho\ \delta\ \alpha]$	$[\omega_x\ \omega_y\ \omega_z]$	$[\psi\ \theta\ \phi]$
I	box, +X [0.0 1.0 0.0] box, -X, ±Y ±Z [0.0 0.0 1.0] panel, +X [0.25 0.25 0.5] panel, -X [1.0 0.0 0.0]	[0 6 0] °/s	[90 0 0] °
II	AA	[3.6 3.6 3.6] °/s	[0 90 0] °
III	as I)	[0 6 0] °/s	[0 0 90] °

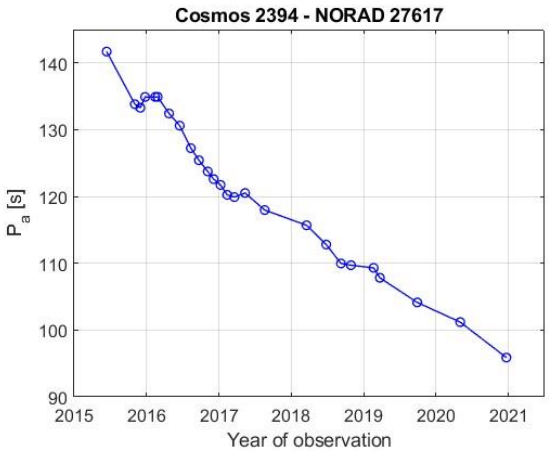

(a)

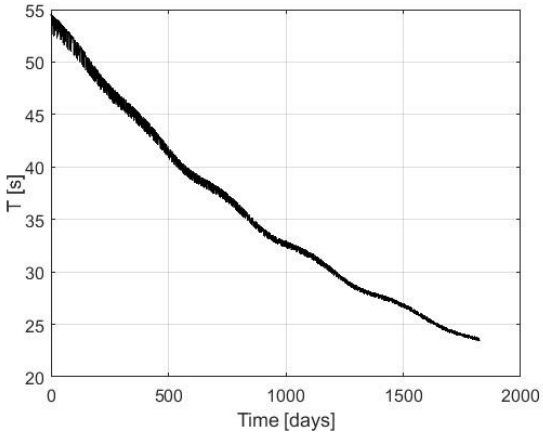

(b)

Figure 10. Apparent spin period of Cosmos 2394 (a) and simulated spin period for test case I (b).

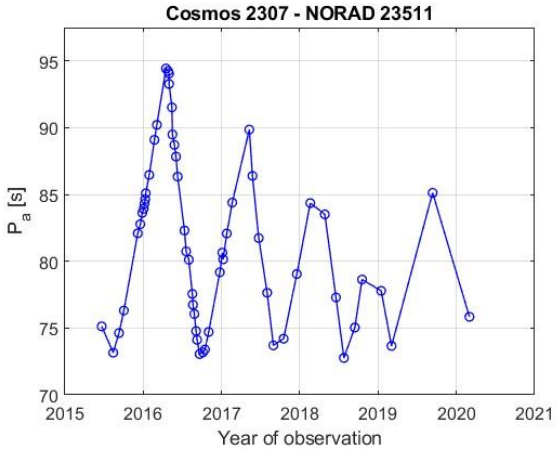

(a)

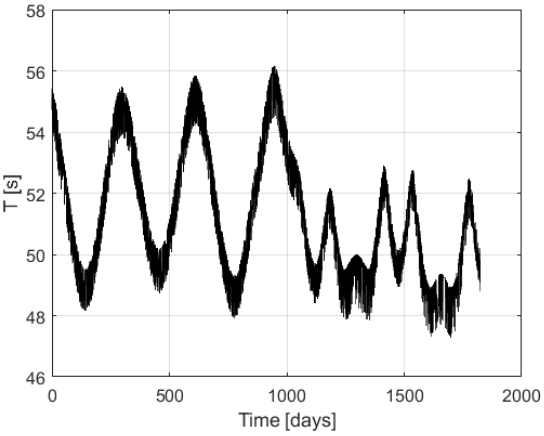

(b)

Figure 11. Apparent spin period of Cosmos 2307 (a) and simulated spin period for test case II (b).

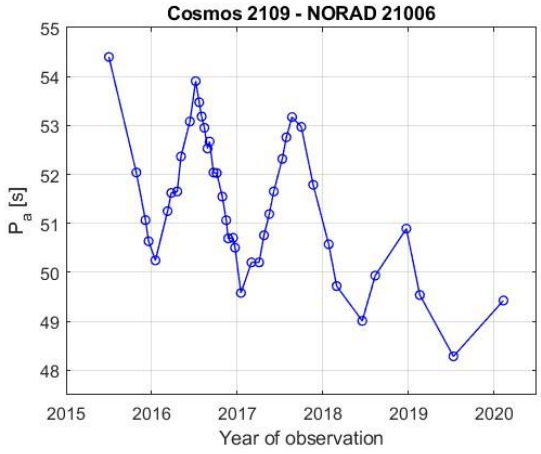

(a)

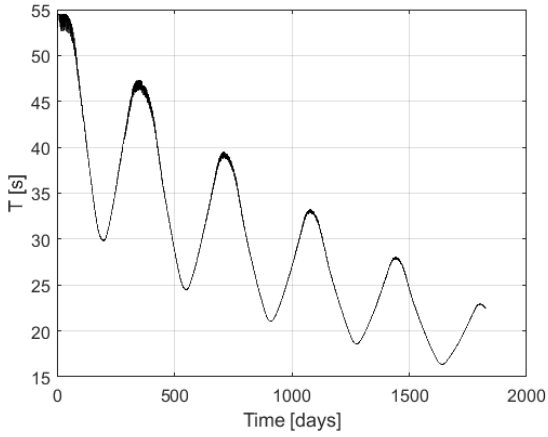

(b)

Figure 12. Apparent spin period of Cosmos 2109 (a) and simulated spin period for test case III (b).

5 CONCLUSIONS

This paper has presented an extensive sensitivity analysis of the long-term time evolution of space debris spin period in MEO focusing on various initial conditions. Initially, symmetric geometries and surface properties have been examined. Regardless of the initial attitude state, the spin period remains bounded around its initial value throughout the propagation period. Introducing asymmetries in the surface properties has impacted only low-speed scenarios, leading to reductions in spin periods of up to 50% compared to the corresponding symmetric surface-properties case.

For box-wing configurations, asymmetries in the canting angle strongly influenced the spin periods. For low-speed cases the spin period decreases significantly; vice versa for the cases in which the initial angular velocity has a component only along the minimum or maximum axis of inertia, the spin period increases. These trends become

more pronounced with larger canting angles. Moreover, although median spin periods remain relatively stable for cases with initial angular velocity along the medium inertia axis (i.e., MeIS), and initial angular velocity components along all the inertia axes (i.e., AllS), the angular velocity patterns change significantly, exhibiting an annual periodicity. Furthermore, introducing asymmetries in surface properties, lead to further increases/decreases in the spin period and, for the MeIS and AllS cases, an additional secular trend of the angular velocity.

Additionally, this study has modelled the spin periods of GLONASS satellites. Three major patterns have been identified in the AIUB database: a monotonic decrease, a yearly periodicity, and a yearly periodicity with secular trend. For each pattern, specific initial conditions that trigger these behaviours in simulation scenarios have been identified.

Discrepancies between observed and simulated data require further analysis to be reduced, including further tuning of the initial conditions, and exploring the effects of other geometric features. Future work shall extend the sensitivity analysis to other orbital regimes and object types.

6 ACKNOWLEDGEMENTS

The authors would like to thank the Swiss National Science Foundation for providing the funds that supported the current study, and all the night observers and the technical staff at the Swiss Optical Ground Station and Geodynamics Observatory Zimmerwald.

7 REFERENCES

1. ESA Space Debris Office. (2024). *ESA's Annual Space Environment Report*. Darmstadt, Germany.
2. Zhang, W., Li, F., Li, J., & Cheng, Q. (2023). Review of On-Orbit Robotic Arm Active Debris Capture Removal Methods. *Aerospace*. https://doi.org/10.3390/aerospace10010013
3. Campbell, J. C., Hughes, K., Vignjevic, R., Djordjevic, N., Taylor, N., & Jardine, A. (2022). Development of modelling design tool for harpoon for active space debris removal. *International Journal of Impact Engineering*, *166*. https://doi.org/10.1016/j.ijimpeng.2022.104236
4. Benvenuto, R., Lavagna, M., & Salvi, S. (2016). Multibody dynamics driving GNC and system design in tethered nets for active debris removal. *Advances in Space Research*, *58*(1). https://doi.org/10.1016/j.asr.2016.04.015
5. Wijayatunga, M. C., Armellin, R., Holt, H., Pirovano, L., & Lidtke, A. A. (2023). Design and guidance of a multi-active debris removal mission. *Astrodynamics*, *7*(4). https://doi.org/10.1007/s42064-023-0159-3
6. Markley, F. L., & Crassidis, J. L. (2014). *Fundamentals of spacecraft attitude determination and control*. *Fundamentals of Spacecraft Attitude Determination and Control*. https://doi.org/10.1007/978-1-4939-0802-8
7. Šilha, J., Pittet, J. N., Hamara, M., & Schildknecht, T. (2018). Apparent rotation properties of space debris extracted from photometric measurements. *Advances in Space Research*, *61*(3). https://doi.org/10.1016/j.asr.2017.10.048
8. Linder, E., Silha, J., Schildknecht, T., & Hager, M. (2015). Extraction of spin periods of space debris from optical light curves. In *Proceedings of the International Astronautical Congress, IAC* (Vol. 3).
9. Larsson, S. (1996). Parameter estimation in epoch folding analysis. *Astronomy and Astrophysics Supplement Series*, *117*(1). https://doi.org/10.1051/aas:1996150
10. Zechmeister, M., & Kürster, M. (2009). The generalised Lomb-Scargle periodogram. *Astronomy & Astrophysics*, *496*(2). https://doi.org/10.1051/0004-6361:200811296
11. Isoletta, G., Opromolla, R., & Fasano, G. (2025). Attitude motion classification of resident space objects using light curve spectral analysis. *Advances in Space Research*, *75*(1), 1077–1095. https://doi.org/10.1016/j.asr.2024.10.034
12. Badura, G. P., Christopher, ·, & Valenta, R. (2024). Physics-Guided Machine Learning for Satellite Spin Property Estimation from Light Curves. *The Journal of the Astronautical Sciences 2024 71:5*, *71*(5), 1–36. https://doi.org/10.1007/S40295-024-00464-5
13. Herzog, J., Schildknecht, T., Hinze, A., Ploner, M., & Vananti, A. (2013). Space Surveillance Observations at the AIUB Zimmerwald Observatory. In *Sixth European Conference on Space Debris, Darmstadt, Germany*.
14. Rachman, A. (2023). *Understanding Attitude Behavior of Inactive GLONASS Satellites using Spin Period Evolution*. PhD Dissertation, Astronomical Institute University Bern, Bern.
15. Rachman, A., Schildknecht, T., & Vananti, A. (2018). Analysis of temporal evolution of debris objects' rotation rates inside AIUB light curve database. In *Proceedings of the International Astronautical Congress, IAC* (Vol. 2018-October).
16. Rachman, A., Vananti, A., & Schildknecht, T. (2020). Understanding the Oscillating Pattern in the

Rotational Period Evolution of several GLONASS Satellites. Retrieved from www.amostech.com

17. Sagnières, L. B. M., & Sharf, I. (2019). Long-term rotational motion analysis and comparison to observations of the inoperative envisat. *Journal of Guidance, Control, and Dynamics*, *42*(2), 364–376. https://doi.org/10.2514/1.G003647

18. Sagnières, L. B. M., Sharf, I., & Deleflie, F. (2020). Simulation of long-term rotational dynamics of large space debris: A TOPEX/Poseidon case study. *Advances in Space Research*, *65*(4), 1182–1195. https://doi.org/10.1016/j.asr.2019.11.021

19. Vallado, D., & McClain, W. (2007). Fundamentals of astrodynamics and applications, 2004. *Space Technology Library, Microcosm Press & Kluwer Academic Publishers*.

20. Curtis, H. D. (2013). *Orbital Mechanics for Engineering Students*. *Orbital Mechanics for Engineering Students*. https://doi.org/10.1016/C2011-0-69685-1

21. Dormand, J. R., & Prince, P. J. (1980). A family of embedded Runge-Kutta formulae. *Journal of Computational and Applied Mathematics*, *6*(1). https://doi.org/10.1016/0771-050X(80)90013-3

22. Space-Track.Org. (n.d.). Retrieved from https://www.space-track.org/auth/login

23. Duan, B., Hugentobler, U., Hofacker, M., & Selmke, I. (2020). Improving solar radiation pressure modeling for GLONASS satellites. *Journal of Geodesy*, *94*(8). https://doi.org/10.1007/s00190-020-01400-9

24. Bury, G., Sośnica, K., Zajdel, R., & Strugarek, D. (2022). GLONASS precise orbit determination with identification of malfunctioning spacecraft. *GPS Solutions*, *26*(2). https://doi.org/10.1007/s10291-021-01221-z

25. Montenbruck, O., Schmid, R., Mercier, F., Steigenberger, P., Noll, C., Fatkulin, R., … Ganeshan, A. S. (2015). GNSS satellite geometry and attitude models. *Advances in Space Research*, *56*(6). https://doi.org/10.1016/j.asr.2015.06.019

26. Revnivykh, S., Bolkunov, A., Serdyukov, A., & Montenbruck, O. (2017). GLONASS. *Springer Handbooks*, 219–245. https://doi.org/10.1007/978-3-319-42928-1_8